Available online at www.sciencedirect.com
ScienceDirect
Journal of Power Sources 175 (2008) 712–723
JOURNAL OF POWER SOURCES
www.elsevier.com/locate/jpowsour

# Microstructure changes in the catalyst layers of PEM fuel cells induced by load cycling Part II. Simulation and understanding

Feng Rong, Cheng Huang *, Zhong-Sheng Liu, Datong Song, Qianpu Wang

*Institute for Fuel Cell Innovation, National Research Council Canada, 4250 Wesbrook Mall, Vancouver, BC, Canada V6T 1W5*

Received 13 July 2007; received in revised form 1 October 2007; accepted 1 October 2007
Available online 9 October 2007

**Abstract**

The microstructure of catalyst layers (CLs) is a naturally random medium and changes in it greatly affect the performance of polymer electrolyte membrane fuel cells. In this paper, the mechanical analysis method, developed in Part I for understanding the mechanism of microstructure changes, is further extended to describe CLs as random three-phase microstructures. Microstructure reconstruction is accomplished using statistical information from experimental images of practical CLs. In the microscopically complex reconstructed microstructure, mechanical analysis is performed in order to understand the mechanism of changes caused by the cycling of start-up and shutdown during operation. Numerical simulation shows that, although different reconstructed microstructures have different changes, there have in common the competition between crack initiations in phases and delamination between different phases in the CLs. This competition plays an important role in microstructure change and results in performance degradation, indicated by the decrease in connection length among different solid components in the CLs after certain duty cycles.


*Keywords:* Microstructure changes; Microstructure reconstruction; Mechanism of degradation; Catalyst layer; PEM fuel cell

## 1. Introduction

The lifetime of the components of polymer electrolyte membrane fuel cells (PEMFCs) has a significant impact on the commercial viability of PEMFCs for both stationary and transportation energy applications [1]. Improvement in their durability can effectively reduce the cost of implementing PEMFC systems. Recently, experimental studies have been undertaken to understand the degradation mechanism of PEMFCs. Many researchers [1–4] believe that microstructure changes in catalyst layers (CLs) can be factors in fuel cell performance reduction. According to experiment results, microstructure changes in CLs include the following: cracks, loss of carbon-supported catalyst clusters, dissolution of recast electrolyte (Nafion ionomer), catalyst particle migration, and agglomerate coarsening [5] These phenomena are obvious especially under dynamic operating conditions (transportation applications). So the microstructure, especially that of CLs, is critical to durability improvement of PEMFCs [4]. There is an urgent need to understand the underlying mechanism of microstructure changes in CLs and how their evolution reduces performance.

Microstructure changes may occur in several ways, such as chemical degradation of the ionic conducting parts or mechanical failure in CLs [5]. Although chemical degradation is a key factor in microstructure changes, it has been suggested that mechanical damage is also highly important [6]. In our companion paper [7], a mechanical analysis model is developed, based on the finite element method, to investigate microstructure changes in CLs. It is found that delaminations and cracks occur between phases in CLs as the effect of duty cycles. The simulation presented in our companion paper [7] is based on a representation of microstructure in CLs, which, although it offers a basic understanding of the changes, suffers from many morphological and associated physical limitations. In addition to the simplicity of the structure, statistical information may

* Corresponding author. Tel.: +1 604 221 3050; fax: +1 604 221 3001.
*E-mail address:* cheng.huang@nrc-cnrc.gc.ca (C. Huang).

0378-7753/$ – see front matter. 
doi:10.1016/j.jpowsour.2007.10.007

deviate from the change in a realistic random porous CL. For instance, the connection area between phases needs to be further enhanced and the components are not as complex as those in a practical three-phase medium [8–10]. To better understand the mechanism of practical random microstructure changes, a reconstruction of random microstructure should be utilized systematically.

In fact, the reconstruction of random media from limited morphological information (statistical distributions, etc.) is an intriguing inverse problem. It is useful to reconstruct CLs using information obtained from a two-dimensional (2D) micrograph or image. A number of approaches have been taken to reconstruct random media [11,12]. Most of them use the filtering method [13] or stochastic optimization [14]. To take full advantage of both of these methods, we will apply them together to reconstruct the microstructure based on the statistical information of CL images.

First, the reconstruction procedure is proposed: statistical feature extraction based on an image process of CLs, initial reconstruction based on the filtering method, and stochastic optimization to refine the results of the filtering method. Second, the method developed in our companion work [7] is extended to investigate the reconstructed microstructure changes. Finally, a basic understanding of the mechanism of microstructure changes in CLs is achieved through mechanical analysis. Moreover, a common indication of performance degradation for different reconstruction results is observed in the simulation results.

## 2. Microstructure reconstruction in CLs

The determination of the macroscopic behaviour of CLs, a random porous medium, can be performed in two steps: generating media with specific geometrical or statistical properties and solving the relevant set of equations. A reconstruction process based on 2D transmission electron microscopy (TEM) experimental images is proposed. In this paper, the whole reconstruction of the microstructure can be divided into three stages: evaluation of phase statistical information, initial reconstruction based on the filtering method, and stochastic optimization reconstruction of the microstructure.

### 2.1. Evaluation of phase statistical information

A common starting point of the reconstruction procedure is the statistical distribution and correlation relationship of phases. For a CL, the phases include the electrolyte (Nafion), the C/Pt agglomerate and pores. We want to generate a random porous CL with volume fractions and correlation functions of components. The CL is assumed to be homogenous and isotropic, although the latter is not essential. First, experimental images are processed to get the statistical information. In this section, one method, based on the physical properties of the different phases in CLs, is proposed to segment the phases in 2D experiment results. In black and white figures, this information is conveyed by the gray value or the intensity of different pixels. So we assume that every pixel represents an individual phase and the intensity of the pixel can be used to indicate its properties. Then three intervals of intensity from 0 to 255 should be determined to distinguish different phases.

The intensity of Nafion is assumed to be greater than that of the C/Pt agglomerate and lower than that of the pores. To determine these two boundary values, the physical properties and mass ratios of the different phases must be used. When the TEM or scanning electron microscopy (SEM) images of a CL are taken, the mass ratio $\varepsilon$, as well as the density $\rho$, of the different phases is known. So the volume ratio ($\delta$) of the different phases can be determined as follows:

$$\delta_1 = 1 - \delta_2 - \delta_3, \qquad \delta_2 = \frac{\rho_{CL}\varepsilon_{Nafion}}{\rho_{Nafion}},$$
$$\delta_3 = \frac{\rho_{CL}\varepsilon_C}{\rho_C} + \frac{\rho_{CL}\varepsilon_{Pt}}{\rho_{Pt}} \tag{1}$$

where $\delta_2$, $\varepsilon_{Nafion}$, and $\rho_{Nafion}$ are volume ratio, mass ratio, and density of Nafion, respectively; $\varepsilon_C$ and $\rho_C$ are the mass ratio and density of carbon, respectively;$\varepsilon_{Pt}$ and $\rho_{Pt}$ are the mass ratio and density of platinum, respectively; $\delta_1$ and $\delta_3$ are the volume ratio of the pores and C/Pt agglomerate, respectively; and $\rho_{CL}$ is the density of the whole CL.

When the CL is assumed to be homogenous, statistical averages can be replaced by volume averages. When it is assumed to be isotropic, these volume averages can be replaced by surface averages. Hence, the use of thin sections is justified. So the volume ratios, which can be regarded as area ratios in the 2D experimental figures, can be used to evaluate the boundaries of intensity. Fig. 1(a), a typical image of a CL by Xie et al. [15], is used to illustrate the process of determining boundaries of intensity. In their fabrication, catalyst inks were prepared by mixing catalyst powder (20 wt% Pt on a Vulcan XC-72, E-TEK), Nafion solution, and isopropanol. The CL in Fig. 1(a) contains 30 wt% Nafion 115. In fact, when Xie et al. [15] were verifying the performance with the macrohomogeneous model, the volume fraction of different compositions in the CL were reproduced based on the constitutive relationship between weight fractions and volume fractions (Eq. (1)); that is, C/Pt:Nafion:pore = 46.7:25.7:27.6. The distribution of the intensity of different pixels is shown in Fig. 1(b). $I_a$ and $I_b$ are the segment phases in the image. Based on the assumption of isotropic random media, area fractions of the CL components should be the same as the volume fractions in the experiments. So $I_a$ and $I_b$ are searched for from 0 to 255 to best approach these area fractions. $I_a$ is determined to be 94 and $I_b$ is 119. In fact, the area fractions of the components, based on intensity, are 43.4:26.7:30.3 (C/Pt:Nafion:pore). When these two values have been determined, Fig. 1(a) can be filtered to a black-and-white figure to indicate different phases, as shown in Fig. 2 where white pixels are the reference phases, specifically (a) pore, (b) Nafion, and (c) C/Pt agglomerate. At this point, the image segmentation has been accomplished based on the mass ratios, densities of components, and intensity of pixels.

As mentioned previously, the presence of different phases in the sample is measured. At each point (pixel) within the experimental sample, an overall phase function $Z(\mathbf{x})$ at each point $\mathbf{x}$ is

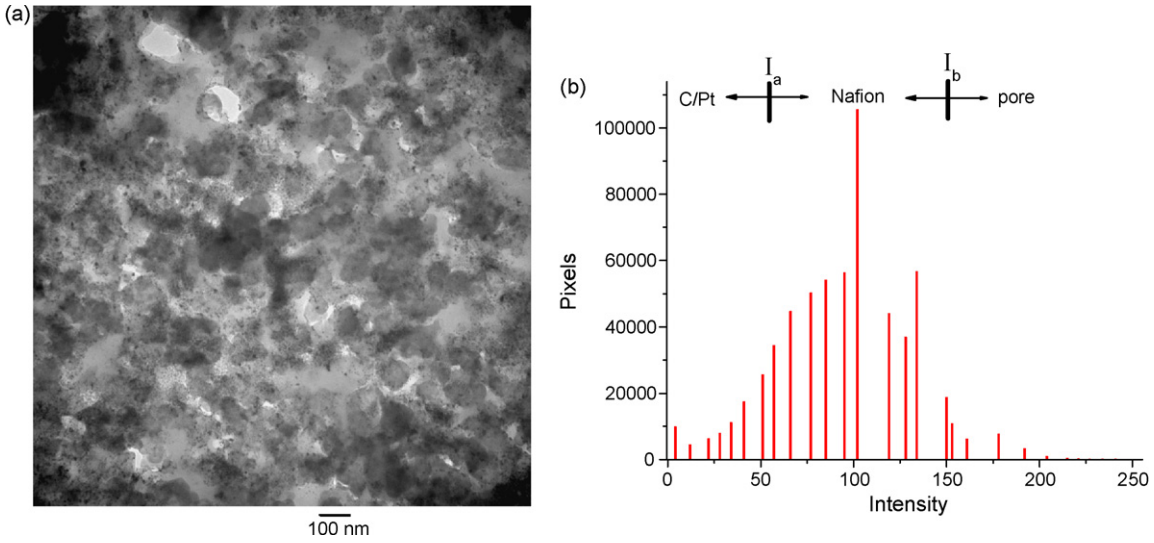


Fig. 1. (a) The TEM image of a cathode CL from Ref. [15] and (b) intensity distribution of the TEM image.

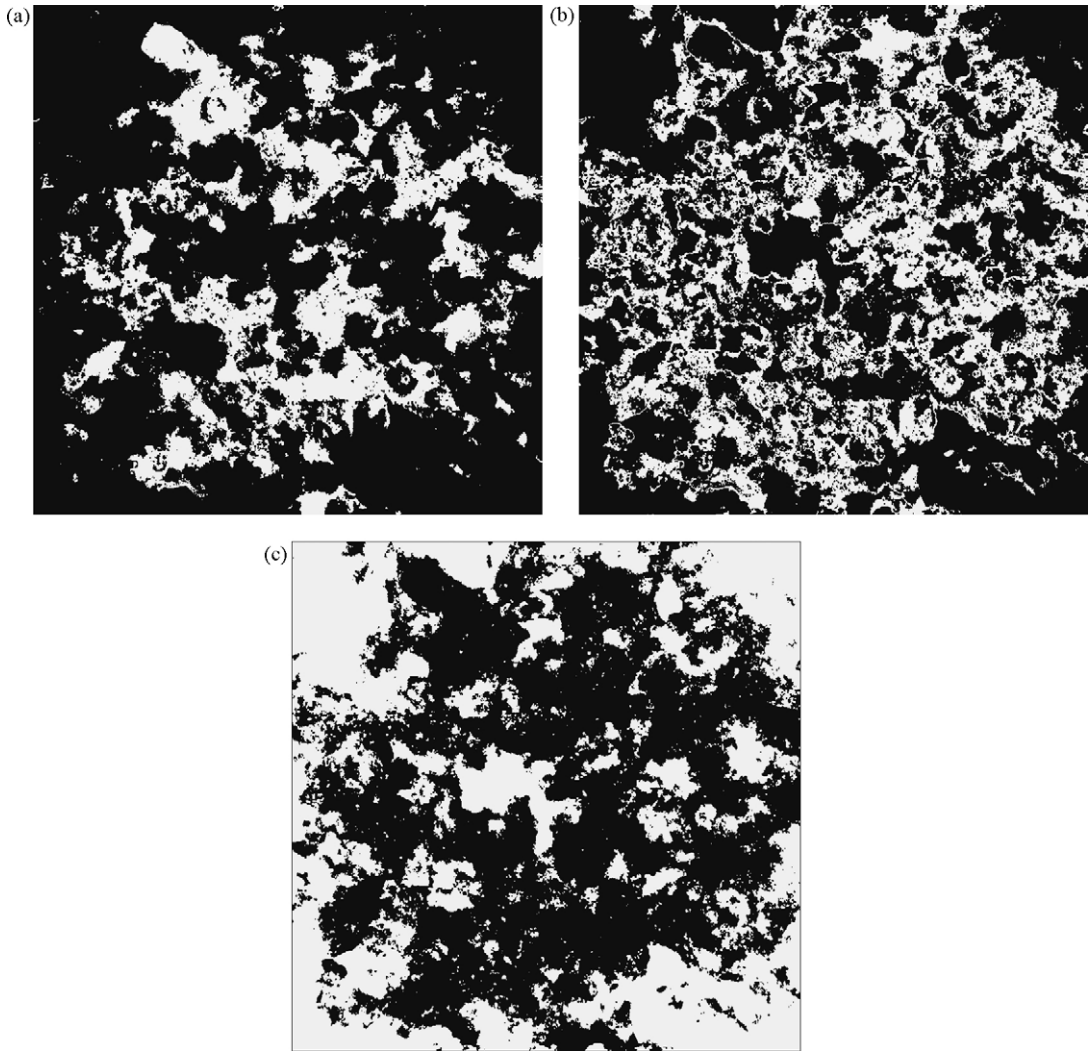


Fig. 2. The segmentation of the TEM image (Fig. 1(a)) based on intensity, where the white pixels are (a) pores, (b) Nafion, and (c) C/Pt agglomerates.

defined as

$$Z(\mathbf{x}) = \begin{cases} \omega_1 & \text{if } \mathbf{x} \text{ belongs to pore} \\ \omega_2 & \text{if } \mathbf{x} \text{ belongs to Nafion} \\ \omega_3 & \text{if } \mathbf{x} \text{ belongs to C/Pt agglomerate} \end{cases} \quad (2)$$

The set of values $\{\omega_k, k=1, 2, 3\}$ is arbitrary; however, in this paper, this set is equal to the sequence of the first three integers $\{0, 1, 2\}$. As $\mathbf{x}$ varies, $Z(\mathbf{x})$ describes a discrete stochastic process. Assuming a homogenous and isotropic medium implies that this process is stationary; that is, it has a constant mean and its autocovariance function is invariant under arbitrary translations. Theoretically, the overall average of $Z(\mathbf{x})$ and the two-point overall correlation function can be introduced as

$$\chi = \overline{Z(\mathbf{x})}$$

$$R_Z(\mathbf{u}) = \frac{\overline{(Z(\mathbf{x}) - \chi)(Z(\mathbf{x}+\mathbf{u}) - \chi)}}{(\overline{Z(\mathbf{x})^2} - \chi^2)} \quad (3)$$

where $R_Z(\mathbf{u})$ is the two-point correlation function, which represents the probability that two points at a distance $\mathbf{x}$ are both the same phase; the overbar denotes the statistical average; and $\mathbf{u}$ is the lag vector. For a statistically homogenous CL, $\chi$ is a constant and $R_Z(\mathbf{u})$ is a function only of the lag vector, $\mathbf{u}$; that is, it is independent of the location vector $\mathbf{x}$. Furthermore, if the CL is isotropic, the correlation function $R_Z(\mathbf{u})$ is a function only of the norm of $\mathbf{u}$.

This is a theoretical declaration of the overall mean and two-point correlation function. It is still necessary to mention the procedure by which they are computed from 2D experimental images of an actual CL. To minimize finite size effects, periodic boundaries and more experimental figures are utilized during evaluation. In Fig. 2, the $M \times N$ (781 × 781) pixels 2D image is defined as a discrete valued function $Z(x, y)$, where $Z(x, y)$ is the same as $Z(\mathbf{x})$ in Eq. (2). The three-phase image $S$ is divided into two halves, $S_1$ and $S_2$, which satisfy $S_1 \cup S_2 = S$ and $S_1 \cap S_2 = \emptyset$. To calculate $R_Z(\mathbf{u})$, $S_1$ is first translated by a distance $u$ along the $x$-axis; it yields $S_1(+u)$. The spatial average indicated in Eq. (3) is replaced by an intersection of images:

$$\overline{Z(x, y)Z(x+u, y)} = S_1(+u) \cap S$$

The other operations indicated in Eq. (3) are then performed algebraically. Fig. 3 shows the result from the three-phase images in Fig. 2. General practical recommendations for the measurements of these correlation functions can be found in Ref. [13].

In addition, it is possible to calculate numerically the inter- and auto-correlations between the different phases from the three-phase images. Theoretically, the three-phase functions $Z_k(\mathbf{x})$ can be defined as

$$Z_k(\mathbf{x}) = \begin{cases} 1 & \text{if } Z(\mathbf{x}) = \omega_k \\ 0 & \text{otherwise} \end{cases}$$

The expected value (denoted by an overbar) of $Z_k(\mathbf{x})$ is the probability of the presence of this phase:

$$\chi_k = \overline{Z_k(\mathbf{x})}$$

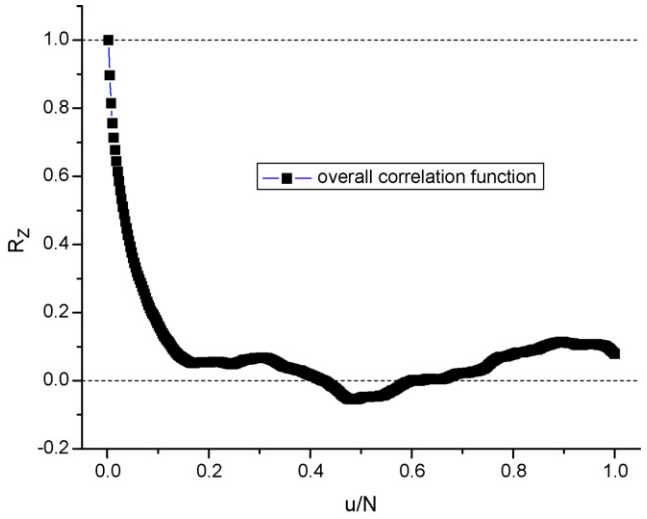


Fig. 3. The global correlation function of the TEM image (Fig. 1(a)).

Here $\chi_k$ should be equal to $\delta_k$ in Eq. (1) if $I_a$ and $I_b$ are determined from $\delta_k$. Notice that $\chi = \sum_{k=1}^{3} \omega_k \chi_k$. The correlation function $R_{Z_k,Z_m}(\mathbf{u})$ is the two-point correlation function, which is the probability that one point at a distance $\mathbf{x}$ belongs to phase $k$ and one point at a distance $\mathbf{x}+\mathbf{u}$ is phase $m$. The definition of $R_{Z_k,Z_m}(\mathbf{u})$ is

$$R_{Z_k,Z_m}(\mathbf{u}) = \frac{\overline{(Z_k(\mathbf{x}) - \chi_k)(Z_m(\mathbf{x}+\mathbf{u}) - \chi_m)}}{\sqrt{(\chi_k + \chi_k^2)(\chi_m + \chi_m^2)}} \quad (k, m = 1, 2, 3) \quad (4)$$

So from three-phase images (Fig. 2), the cross- and auto-correlation relationship can be calculated, as shown in Fig. 4 where (a) is the auto-correlation functions and (b) is the cross-correlation functions between phases.

In this section, the segmentation of a gray image of an actual CL is performed based on mass ratios and physical constants of the components. In addition, the global correlation function, as well as functions between phases, can be calculated.

### 2.2. Initial reconstruction based on the filtering method

The reconstruction of microstructure in CLs can be achieved based on feature extraction of an actual three-phase CL. We seek to generate a random porous microstructure containing three phases, each having a specified volume fraction $\delta_k$. The overall correlation function $R_Z(\mathbf{u})$ is given (Eq. (3) and Fig. 3). An extensively examined reconstruction method, called the filtering method, is based on successively passing a normalized uncorrelated random Gaussian field through first a linear and then a nonlinear filter to yield the discrete values, which represent the phases of the structure. In this section, the filtering method is used to reconstruct an initial value for subsequent stochastic optimization. The reason for this will be discussed at the end of this section.

Reconstructing a three-phase medium is done by thresholding a continuous Gaussian field. The initial reconstructed

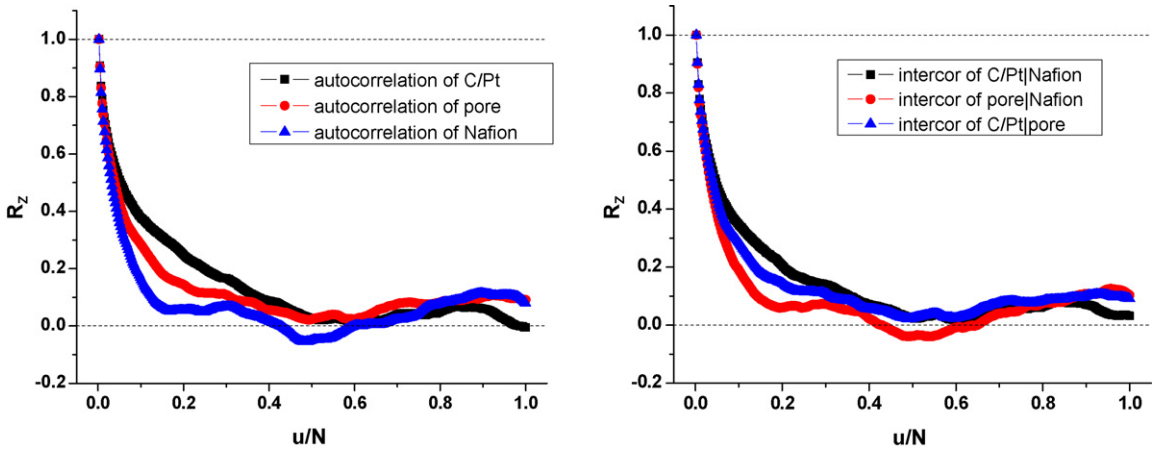


Fig. 4. The cross- and auto-correlation relationships of TEM image (Fig. 1(a)).

microstructure consisting of a Gaussian distributed random field $X$ is generated using Marsaglia's ziggurat algorithm [16], as shown in Fig. 5(a). This independent Gaussian field $X$ is convoluted by one constructed linear filter and forms another field $Y$ that is still Gaussian distributed but correlated. The nonlinear filter then performs a threshold cut to the field $Y$ to generate the final reconstructed structure $Z$. The following will gives the construction and influence of these filters and relates their properties to the statistical properties of the resulting fields. The construction of filters is called an inverse problem by Losic et al. [17]. For practical purposes, the porous microstructure is constructed in a discrete manner. It is considered to be composed of $N_x \times N_y$ (in Fig. 5(a), $N_x = N_y = 200$) small squares, each of the same size $a$. These elementary squares are filled with either voids, Nafion, or C/Pt agglomerate. Hence, the spatial variables $\mathbf{x}$ and $\mathbf{u}$ in Eqs. (3) and (4) will take only discrete values; the corresponding trios of integers are denoted by

$$x = (i, j) * a \quad \text{and} \quad u = (r, s) * a, \quad i, r \in [1, N_x]; \quad j, s \in [1, N_y] \tag{5}$$

Moreover, a set of strictly increasing constants $\{b_i, i = 0, 1, \ldots, n\}$ with $b_0 = 0$ and $b_n = 1$ is constructed. It partitions the interval [0, 1] into $n$ segments $I_i = [b_{i-1}, b_i]$, $I = 1, 2, \ldots, n$. Accordingly, the set $\Re$ of real numbers is partitioned into the family of interval

$$J_i = [\Phi^{-1}(b_{i-1}), \Phi^{-1}(b_i)] \tag{6}$$

where $\Phi(y)$ is the Gaussian probability distribution function (PDF); that is,

$$\Phi(y) = \frac{1}{\sqrt{2\pi}} \int_{-\infty}^{y} \exp\left(-\frac{t^2}{2}\right) \mathrm{d}t \tag{7}$$

A value of $\omega_k$ among the possible values of $Z$ in Eq. (2) is associated with each of these segments $J_i$; that is, each part is considered to belong to one of three phases. Note that $n$ can be larger than three, but is not necessarily equal; several zones can correspond to the same phase.

The most difficult point is the determination of the linear filter. One can start from the fact that the random vector $(Y(\mathbf{x}), Y(\mathbf{x}+\mathbf{u}))$, after a filter is applied, is a bivariate Gaussian whose probability density is known; this density can be expanded in terms of Hermite polynomials. After some systematic manipulations, which use classical identities [18], the target correlation function $R_Z(\mathbf{u})$ can be expressed as a series in terms of the correlation function of $Y$, $R_Y(\mathbf{u})$:

$$R_Z(\mathbf{u}) = \sum_{m=0}^{\infty} C_m^2 R_Y^m(\mathbf{u}) \tag{8}$$

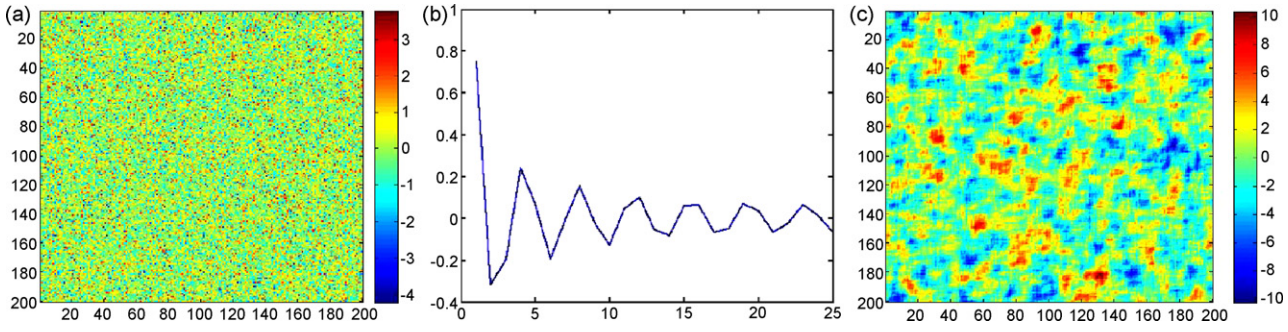


Fig. 5. (a) Uncorrelated Gaussian distributed random field. Here $N_x = N_y = 200$; (b) coefficients of linear filter; (c) correlated Gaussian distributed random field after linear filter applied.

The coefficients $C_m$ are given by

$$C_m = \frac{1}{\sqrt{2\pi m!}\sigma_z}\sum_{i=1}^{n}\omega_i \int_{\Phi^{-1}(b_{i-1})}^{\Phi^{-1}(b_i)} \mathrm{e}^{-(y^2/2)} H_m(y)\,\mathrm{d}y$$

where $\Phi(y)$ is the Gaussian PDF (Eq. (7)), $b_i$ is the strictly increasing constants set defined in Eq. (6), $\sigma_z$ is the square root of the variance of the random variable $Z$ and $H_m(y)$ are Hermite polynomials. They may be expressed as

$$\sigma_z^2 = \left(\sum_{k=1}^{3}\chi_k\omega_k^2\right) - \left(\sum_{k=1}^{3}\chi_k\omega_k^2\right)^2$$

$$H_m(y) = (-1)^m \exp\left(\frac{y^2}{2}\right)\frac{\mathrm{d}^m}{\mathrm{d}y^m}\left(\exp\left(-\frac{y^2}{2}\right)\right)$$

When $\chi_k$ is given from Section 2.1, the correlation function $R_Y(\mathbf{u})$ is easily derived from $R_Z(\mathbf{u})$, based on Eq. (3). This simply corresponds to the numerical inversion of Eq. (8) by any standard method. In our reconstruction, an algorithm developed by Dekker [19] uses a combination of bisection, secant, and inverse quadratic interpolation methods.

Once $R_Y(\mathbf{u})$ is known, the linear filter may be constructed. A linear operator can be defined by an array of coefficients $c(\mathbf{v})$, where $\mathbf{v}$ belongs to a finite square $[0, L_c]^2$ in $Z^2$. Outside this square, it is equal to 0. A new random field $Y(\mathbf{x})$ can be expressed as a linear combination of the uncorrelated Gaussian random variables $X(\mathbf{x})$,

$$Y(\mathbf{x}) = \sum_{v\in[0,L_c]^2} c(\mathbf{v})X(\mathbf{x}+\mathbf{v}) \tag{9}$$

Their correlation function $R_Y(\mathbf{u})$ is easily seen to be

$$R_Y(\mathbf{u}) = \sum_{v\in[0,L_c]^2} c(\mathbf{v})c(\mathbf{v}+\mathbf{u}) \tag{10}$$

if the variance of $Y(\mathbf{x})$ is equal to 1.

For isotropic media and the discretization of microstructure (Eq. (5)), the number of coefficients $c$ in the linear filter can be greatly reduced since $c$ is now a function of only the distance

$$c(\mathbf{v}) = c(r,s) = c(\sqrt{r^2+s^2}) = c(d) \tag{11}$$

where $d$ is the distance. Substituting Eq. (11) into Eq. (10), one can determine the function $c$ from nonlinear equations:

$$\sum_{v\in[0,L_c]^2} c(\sqrt{r^2+s^2})c(\sqrt{(r+u)^2+s^2}) = R_Y(u) \tag{12}$$

In our simulation, the nonlinear least squares curve-fitting algorithm is utilized to obtain the coefficients $c$ in the linear filter from Eq. (12). The coefficients $c$ are shown in Fig. 5(b).

The random field $Y(\mathbf{x})$ (shown in Fig. 5 (c)) is correlated after the linear filter (Eq. (9)) is applied. But this is still not satisfactory since it takes its value in $\Re$, while the CL must be represented by a three-valued field $Z(\mathbf{x})$. In order to extract such a field from $Y(\mathbf{x})$, a nonlinear filter $G$ is applied; that is, the random variable $Z$ is a deterministic function of $Y$, $Z = G(Y)$. When the value $y$ of the random variable $Y(\mathbf{x})$ falls within the interval $J_i$ (Eq. (6)), $Z$ is set to the corresponding value $\omega_i$

$$Z = G(Y) = \omega_i \quad \text{if } y \in J_i$$

Obviously, the probability of each $\omega_i$ is equal to $\chi_k$ if the following condition is fulfilled

$$\sum_{\omega_i=\omega_k}(b_i - b_{i-1}) = \chi_k$$

At this point, the nonlinear filter is constructed to correlate the random field in $\Re$ to the three-phase field $Z$, which is the reconstruction of the microstructure. Fig. 6(a) shows the result after the nonlinear filter is applied to Fig. 5(c). The overall correlation function of Fig. 6(a) can be evaluated based on the method proposed in Section 2.1, as shown in Fig. 6(b). It can be seen that the difference between the reconstructed and target correlation functions is relatively small, especially in the short-range correlation.

In the previous filtering method, the only correlation imposed on the process is the global correlation function (Eq. (3)). Hence, the cross-correlation relationship between the different phases in the reconstructed media should be examined to verify the

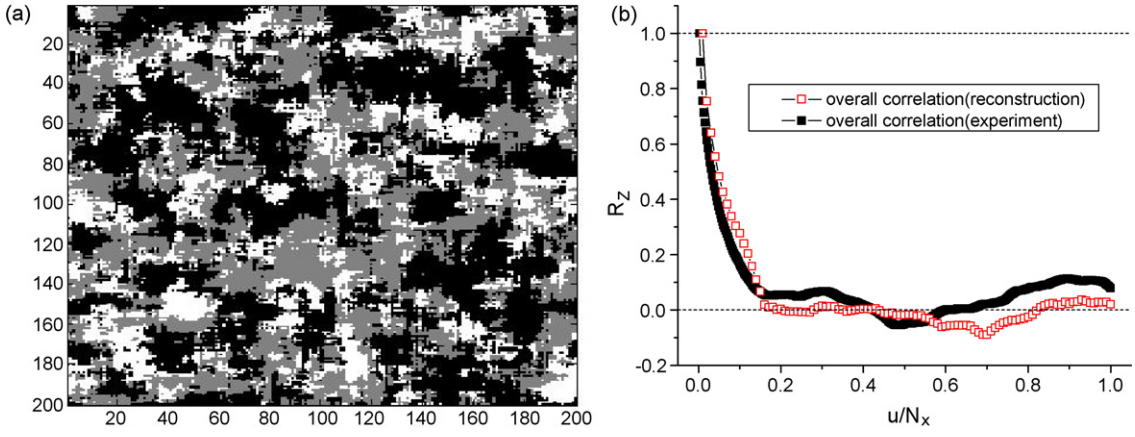


Fig. 6. (a) Three-phase reconstructed microstructure (black pixels represents C/Pt agglomerate, gray pixels are Nafion and white are pore); (b) overall correlation function of reconstructed microstructure.

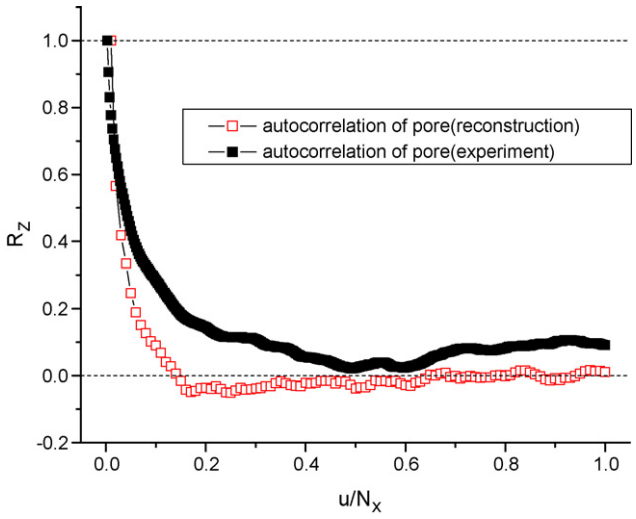


Fig. 7. The auto-correlation relationship of pore in both reconstructed microstructure and experimental image.

results. The auto-correlation of pore phases is calculated according to Eq. (4) and Fig. 6(a) and shown in Fig. 7. Although the trend of auto-correlation functions between different phases follows that of experimental ones, there are clearly noticeable discrepancies between them. This can be considered to be one of drawbacks of using the filtering method to reconstruct multiple-phase microstructure.

In fact, it should be emphasized that there are several artificial parameters introduced in the filtering method: the size of the generated microstructure $N_x$ and $N_y$, the cutoff maximum $m$ in the infinity series of the linear filter (Eq. (8)), the length of the linear filter's square $L_c$ (Eq. (9)), and number of segment intervals in [0, 1] $n$ for constructing the nonlinear filter. These parameters dramatically influence the reconstruction of the microstructure [13] and are also a key problem of the filtering method for reconstruction.

Moreover, it is difficult to extend the Gaussian filtering method to incorporate non-Gaussian statistics. Hence the method is model-dependent; that is, it depends on the underlying Gaussian statistics. So in our proposed reconstruction, the results of the filtering method are used as the initial value for stochastic optimization for reconstruction.

### 2.3. Stochastic optimization for reconstruction

Clearly, the filtering method with the conventional overall correlation function alone may not be adequate to characterize the microstructure of multiphase media for accurate reconstruction. It is desirable that a reconstruction procedure has the ability to incorporate as much crucial microstructure information as possible to capture the salient features of the reference structure.

Recently, Torquato et al. [12,20–22] developed a reconstruction procedure based on a stochastic optimization technique. Starting from an initial realization of the random medium, the method proceeds to find a realization in which the calculated correlation functions best match the target functions. This is achieved by minimizing the sum of squared differences between the calculated and target functions via a stochastic optimization technique, such as the simulated annealing method [14].

Although the filtering method has several disadvantages, it gives us a good starting point for reconstruction. So in this paper, stochastic optimization starts from the reconstruction of the filtering method. The advantage of this initial value of optimization will be presented at the end of this section. Now, we will focus on the key points of stochastic optimization for the reconstruction of microstructures in CLs.

Consider the reference (experimental) three-phase cross-correlation functions $R_{Z_k,Z_m}$ ($k, m = 1, 2, 3$) of a CL presented in Section 2.1 and calculated from the 2D experimental images. Let $\widehat{R}_{Z_k,Z_m}$ be the corresponding correlation function of the reconstructed microstructure (with periodic boundary conditions) at some time step. It is this microstructure that we will attempt to evolve towards $R_{Z_k,Z_m}$ from the reconstruction result of the filtering method.

At any particular time step, a fictitious energy $E$ can be defined as

$$E = \sum_{u} \sum_{k,m} [\widehat{R}_{Z_k,Z_m}(\mathbf{u}) - R_{Z_k,Z_m}(\mathbf{u})]^2$$

where the sum of $\mathbf{u}$ is over all discrete values of the generated microstructure (Eq. (5)) and the indexes $k$ and $m$ denote the type of the different phases. To evolve the microstructure towards $R_{Z_k,Z_m}$ (i.e., minimizing $E$), we interchange the states of two arbitrarily selected pixels of different phases, automatically preserving the volume fraction of both phases. After the interchange is performed, the new energy $E'$ and the energy difference $\Delta E = E' - E$ can be calculated. This phase interchange is then accepted with some probability $p(\Delta E)$ that depends on $\Delta E$. Here the probability is given by the Boltzmann distribution; that is, the Metropolis acceptance rule [20]

$$p(\Delta E) = \begin{cases} 1 & \Delta E \leq 0 \\ \exp(-\Delta E/T) & \Delta E > 0 \end{cases}$$

where $T$ is a fictitious temperature. This is the concept of a simulated annealing schedule. The cooling or annealing schedule, which governs the value and rate of change of $T$, is chosen to be sufficiently slow to allow the system to evolve to the desired state as quickly as possible without trapping in any local energy minima (metastable states). At each annealing step $k$, the system is allowed to evolve long enough to thermalize at $T(k)$. The temperature is then lowered according to a prescribed annealing schedule $T(k)$ until the energy of the system approaches its ground state value within an acceptable tolerance.

In our reconstruction procedure, the system evolves through the logarithmic annealing schedule, which decreases the fictitious temperature to the ground state according to $T(k) \sim 1/\ln(k)$. A logarithmic decrease may cause very slow convergence. Thus, for practical purposes, we adopt the more popular and faster annealing schedule $T(k)/T(0) = \lambda^k$, where the constant $\lambda$ is the annealing rate which must be less than butclose to 1 and assumed before annealing. More detail can be found in Ref. [14].

As a matter of fact, the optimization problem normally faces the same challenge, the sensitivity of the initial value.

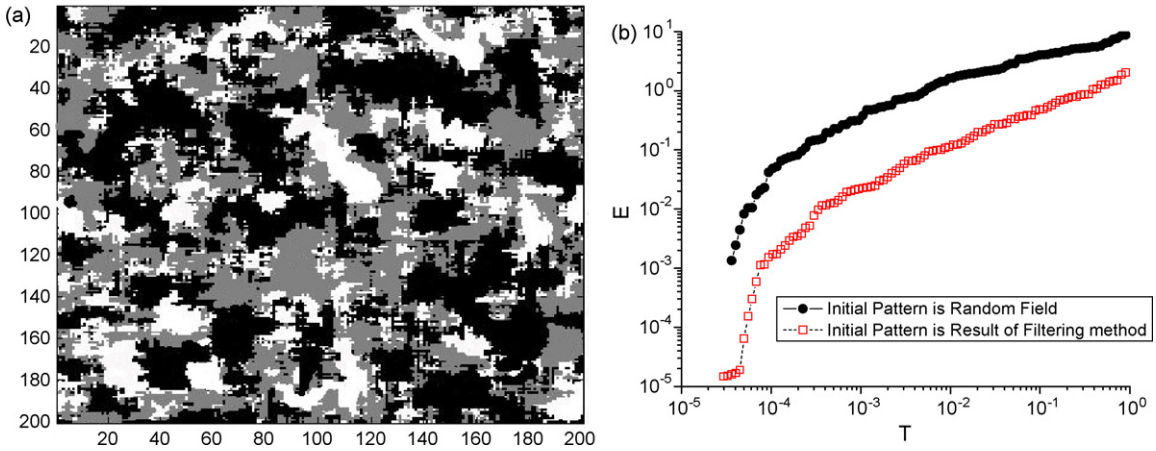


Fig. 8. (a) Microstructure reconstruction after stochastic optimization (initial pattern is Fig. 12(a), black pixels represent C/Pt agglomerate, gray pixels are Nafion, and white are pore); (b) "temperature" dependence of configuration energy.

The character of the energy landscape determines how closely one can numerically approach the true global minimum. In general, bad initial values of optimization will result in both local metastable states and meaningless computation time. To avoid this effect, two kinds of reconstruction are proposed. One starts from a random three-phase pattern, while the other is based on the result of the filtering method (Fig. 6(a)). In the latter, the result of the filtering method is chosen as the initial value of stochastic optimization and it has been verified that the overall correlation function (Fig. 6(b)) recurs the target one better. Fig. 8(a) shows the result of stochastic optimization.

Fig. 8(b) shows the "temperature" dependence of configuration energy $E$. The optimization computational time cost of the initial random pattern is 18,061.31 s while, if we start from the result of the filtering method, the computational time is about one fourth of that (i.e., 4615.22 s). These reconstructions show the advantages of using the results from the filtering method. Doing so makes the energy less than the random initial value and saves computational time.

Moreover, the lower order correlation functions do not contain complete morphological information and thus they cannot uniquely characterize the microstructure, even if the global minimum is achieved. The generated microstructures do not necessarily contain the same statistical information beyond what is imposed, even though a naked-eye comparison is many times more insensitive to such differences. So we reconstruct five different microstructures (Fig. 9, $N_x = N_y = 20$) to understand the mechanical mechanism of microstructure changes due to environmental change. According to Fig. 9(f), the correlation

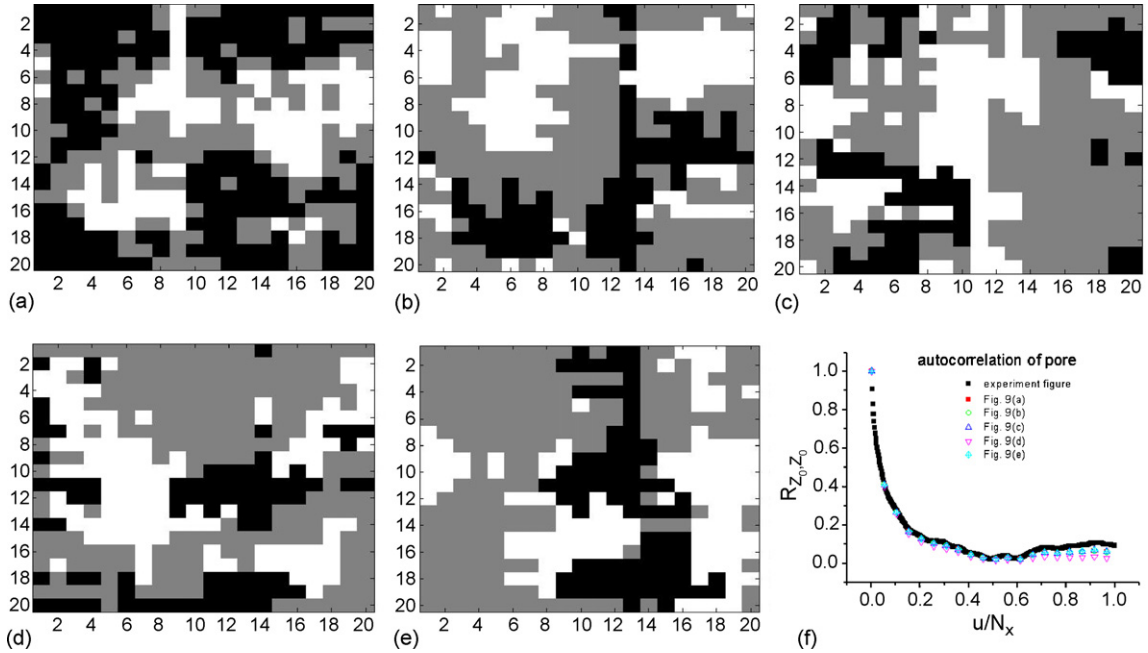


Fig. 9. (a)–(e) Five different microstructure reconstructions used to simulate the microstructural changing ($N_x = N_y = 20$, black pixels represent C/Pt agglomerate, gray pixels are Nafion, and white are pore); (f) the auto-correlation relationship of pore in these reconstructed microstructures and experimental image.

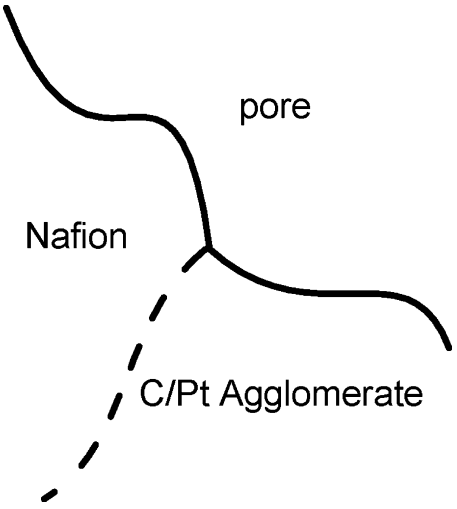


Fig. 10. Different phases in CLs, where the dashed line is the boundary of Nafion and the C/Pt agglomerate, and solid lines are the boundaries of pore and the other two components.

functions of pores in these microstructure reconstructions are good estimators of that of the experimental image.

In summary, the microstructure in CLs is recurred through a reconstruction procedure. Firstly, the experimental image is analyzed and the correlation functions of phases are extracted as the target of reconstruction. Secondly, the filtering method is utilized to give us the initial estimation of reconstruction. Finally, the stochastic optimization is applied to get the final reconstruction.

## 3. Mechanical analysis of microstructure changes

As indicated in Section 2, the reconstruction process is based on the experimental work of Xie et al. [15]. Based on the experimental TEM images of CLs after fabrication, the reconstruction is processed with the stochastic optimization method.

Once the microstructure is reconstructed and the constituent phases (i.e., carbon/catalyst agglomerate, pore, and electrolyte phases) are identified, the mechanical analysis can be performed on the reconstructed CL. The mechanical analysis model, developed for fictitious microstructure changes in our companion paper [7], is extended here to investigate the changes in reconstructed microstructure due to environmental change, such as thermal and humidity cycles during the start-up and shutdown of the fuel cell.

As indicated in Fig. 10, there are three different phases in CLs: electrolyte (Nafion), pore, and carbon/catalyst (Pt) agglomerate. In our model, two components (Nafion and the C/Pt agglomerate) are meshed in the domain for the sake of the finite element method. The pore phase is considered as void in the solid. To simulate the mechanical response of Nafion and the C/Pt agglomerate, the rate-independence constitutive relationship is applied to depict the relationship between the force and deformation in them. It is assumed that the carbon and platinum have a linear-elastic behaviour and do not swell in response to moisture. Based on many mechanical experimental results, the piecewise linear isotropic elastic-plastic-failure model (Fig. 11(a)) is proposed to describe the behaviour of Nafion. The parameters in the model are Young's modulus $E_0$, plastic modulus $E_1$, static yield stress $\sigma_{p0}$, and failure stress $\sigma_s$. These parameters depend on changes in moisture and temperature. Two-dimensional interpolation is used to obtain all data between discrete experimental data points. Young's modulus $E_0$, for example, is shown in Fig. 11(b) and the following

$$\frac{E_0}{E_{0\mathrm{r}}} = \left[1.9\left(\frac{\mathrm{RH}}{\mathrm{RH_r}}\right)^2 - 20.2\left(\frac{\mathrm{RH}}{\mathrm{RH_r}}\right) + 57500\right] \times \left(0.023\left(\frac{T}{T_\mathrm{r}}\right)^2 - 0.213\left(\frac{T}{T_\mathrm{r}}\right) + 387\right)$$

where $\mathrm{RH_r}$, $T_\mathrm{r}$, and $E_{0\mathrm{r}}$ are the reference values of humidity, temperature, and Young's modulus, respectively. The reference Young's modulus is input as the value (226.2 MPa) at 30% RH and 25 °C. The other parameters can be found in our companion paper [7].

In addition, to simulate the debonding phenomena (or delamination) between Nafion and the C/Pt agglomerate, the cohesive

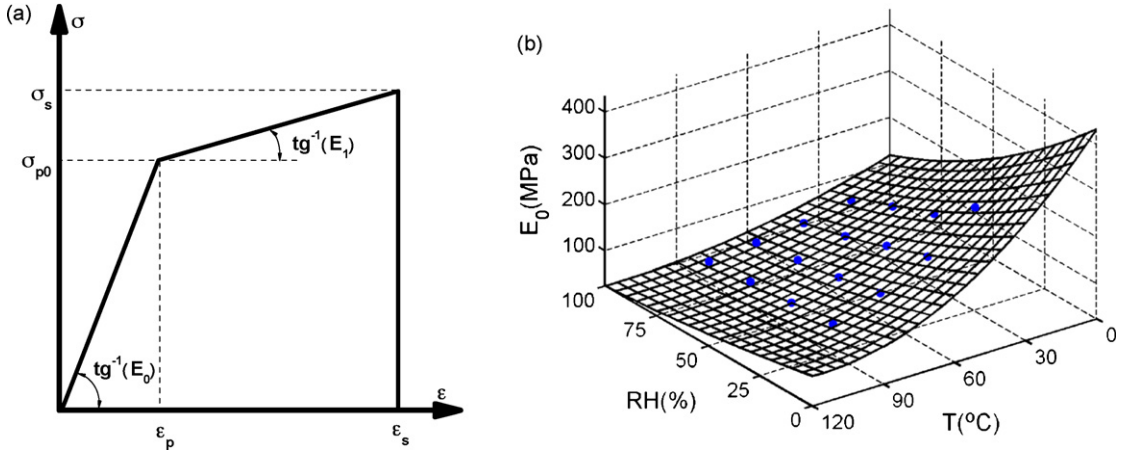


Fig. 11. (a) The piecewise linear constitutive relationship of Nafion adopted in the model; (b) Young's modulus as functions of temperature and relative humidity.

zone model (CZM) is applied to mimic the boundary of these two phases, indicated as a dashed line in Fig. 10. The CZM is, in fact, a model that adopts softening relationships between forces and separations, which in turn introduce a critical fracture energy that is also the energy required to break apart the interfaces. The parameters in the CZM can be determined through the empirical relationship between the boundary and bulk material. It should be mentioned that the constitutive relation for each cohesive surface is taken to be elastic so that any dissipation associated with separation is ignored. So the failure of CZM elements is manually considered when the strain in the CZM exceeds one initial strain strength for the statistics of interface failure between Nafion and the C/Pt agglomerate; that is, for one CZM element, if

$$\max\left(\frac{\delta_n}{\bar{\delta}_n}, \frac{\delta_t}{\bar{\delta}_t}\right) > c_0 \tag{13}$$

the element is considered to be a failed one. Here $\delta_n$ is the normal separation across the interface, $\delta_t$ is the shear separation along the interface, $\bar{\delta}_n$ is the normal separation where the maximum normal traction is attained with $\delta_t = 0$, $\bar{\delta}_t$ is the shear separation where the maximum shear traction is attained at $\delta_t = \bar{\delta}_t/\sqrt{2}$; and $c_0$ is the coefficient corresponding to the maximum strain of interfaces.

When fuel cells start-up and shutdown, the humidity and temperature in the CLs will change, and the Nafion will swell or shrink. Therefore, the Nafion will come into contact with the C/Pt agglomerate or with another Nafion domain. So, the contact model is used on the boundary between the pore and the other two components (solid lines in Fig. 10). All of these contact pairs include the effect of friction, in which the coefficient of friction is determined through experiment [23]. It should be noted that these contacts have no stickiness; that is, when the normal force across the interface is traction, the contact phenomenon will disappear.

In summary, the finite element method, with the support of the CZM and the frictional contact model, is proposed to obtain the mechanical response of CLs. The parameters in the CZM and the contact model can be determined from the empirical relation, as done in Part I. With the finite element method simulation, the underlying mechanism of the changes of the reconstructed microstructure can be understood.

## 4. Mechanism of reconstructed microstructure changes

According to observations, cracks and delamination can be found in the aging CLs of PEM fuel cells. The finite element method, along with the CZM and the frictional contact model [7], is proposed for the investigation of mechanical degradation of CLs under hydrothermal cycles, simulating the start-up and shutdown of PEM fuel cells.

The temperature and humidity profiles come from Ref. [24]. The driving forces behind the simulation are the cycled changes of relative humidity (RH) and temperature ($T$), as shown in Fig. 12 where the initial phase difference between the RH cycle and the $T$ cycle is $t_0 = 2$ s, and the period of humidity and temperature are $t_{RH} = t_T = 400$ s. The maximum and minimum relative humidity are $RH_{max} = 90\%$, and $RH_{min} = 30\%$, respectively. The maximum and minimum temperature are $T_{max} = 85\,^{\circ}C$ and $T_{min} = 25\,^{\circ}C$, respectively.

The 2D reconstruction of the microstructure in CLs was shown in Fig. 9. This problem is also considered to be a plane strain problem because the thickness of CLs is much smaller than the planar dimension.

The commercial software ANSYS is used to conduct the simulations. The data used to simulate the reconstructed CL come from the results of stochastic optimization for reconstruction. At the beginning of analysis, the topology of the microstructure is modified because of constraints and singularity. Although these modifications are very small, especially in cases with large samples (i.e., for large $N_x$ and $N_y$), they are very important to the convergence of computation.

The mesh is done in ANSYS and shown in Fig. 13. The periodic boundary condition is applied on the four boundaries of the whole computational domain to avoid the effect of size. To simulate the interface effect between Nafion and the C/Pt agglomerate, the CZM is used on the boundary between them. The frictional contact model is used to simulate the contact phenomenon.

Based on this simulation, Fig. 14 shows the evolution of both delamination fracture energy and plastic Mises strain. Fig. 14(a) shows two areas which will be examined more closely in Fig. 14(b) and (c) to investigate the delamination energy and plastic strain, respectively. When the humidity and temperature begin to increase, the Nafion swells and delamination fracture energy accumulates. When Eq. (13) is satisfied as the result of fracture energy accumulation in one element, this element is considered to be the failure one. So as Fig. 14(b) shows, the

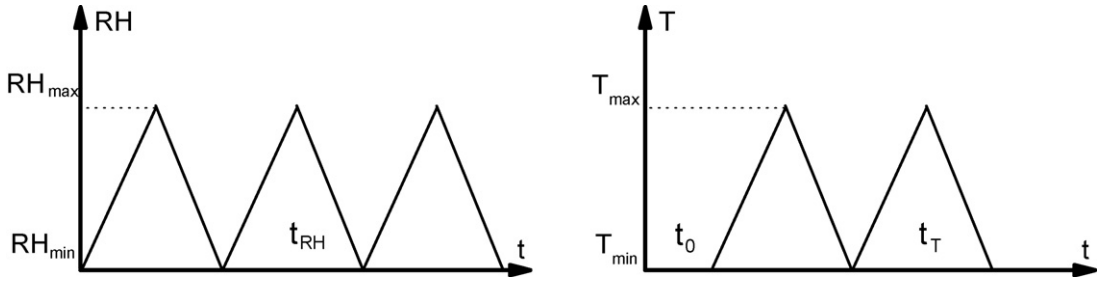


Fig. 12. The schematic graph of relative humidity and temperature cycled change.

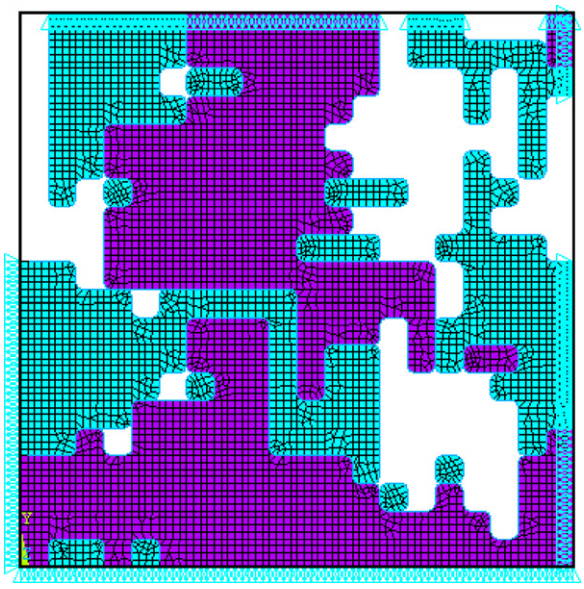

Fig. 13. Mesh result of reconstructed microstructure with symmetric boundary condition.

element (indicated with di) at the triple boundary of Nafion, C/Pt agglomerate, and pore failed at 60 s. Meanwhile, the plastic strain accumulates in the Nafion. At 1612 s, there was crack initiation in the Nafion (as indicated with ci in Fig. 14(c)). Therefore, as humidity and temperature cycle, the plastic strain accumulates in the Nafion, resulting in fatigue (Fig. 14(c)). Thus there is competition between the Nafion's yield failure and Nafion-C/Pt agglomerate delamination because of the cyclic environmental changes.

As we know, the microstructure based on stochastic optimization is not unique; that is, a single microstructure cannot be determined by a few lower order correlation functions, perhaps because optimization is not the true global minimum and the optimization process is sensitive to the initial pattern of reconstruction. So different microstructures should be simulated to investigate the common underlying mechanism of microstructure changes in CLs.

However, many factors in the microstructure have complex influences on the electrochemical performance of fuel cells. Phase connectivity is one of them. Here *phase connectivity* means the interface between different solid phases in CLs. It is the key factor in determining effective contact area, effective chemical reaction rate, and percolation limits. In experiments, it is hard to observe the evolution of these interfaces. However, from the mechanical analysis, the interfaces between Nafion and the C/Pt agglomerate can be determined by simply calculating the contact length between them.

Five different microstructures (Fig. 9) were simulated under cyclic changes of humidity and temperature. The accumulation of both delamination energy and plastic energy were observed in these simulations. The competition between the accumulation of delamination energy and the accumulation of plastic strain (energy) plays a key role in microstructure changes.

As a result of the simulation results for these five different microstructures, the phase connectivity can be measured after several cycles, as shown in Fig. 15, where $\Delta L$ represents the change in the length of the interface between Nafion and the C/Pt agglomerate. An increase in $\Delta L$ means a decrease in the interfaces between Nafion and the C/Pt agglomerate. The connectivity decreases by more than 3% of the whole initial phase

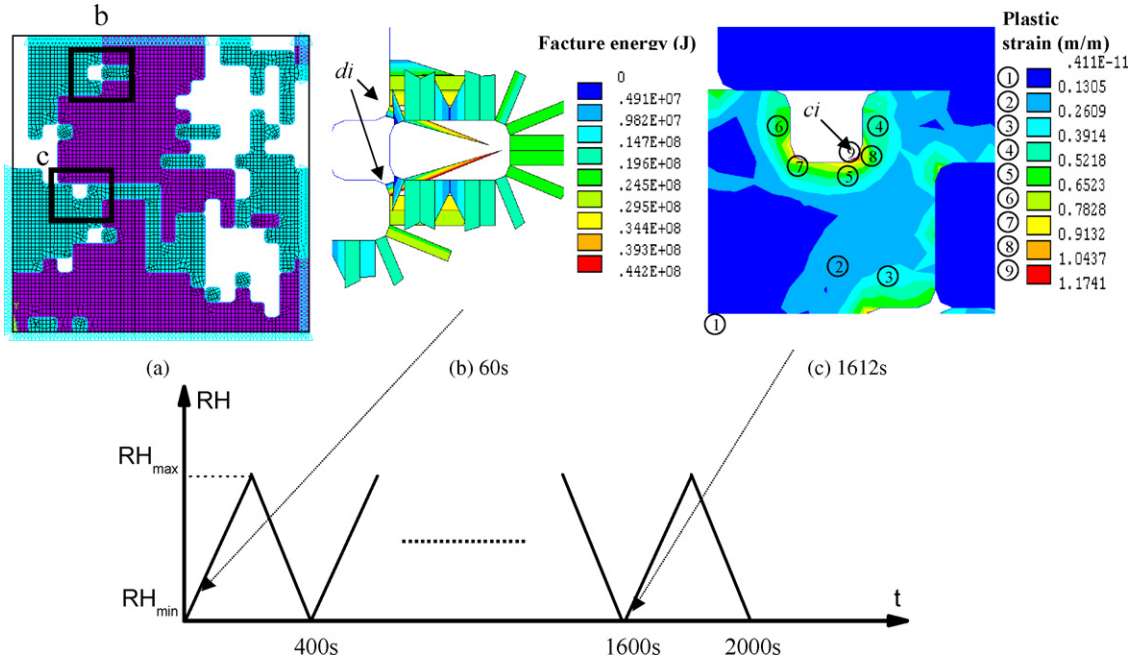


Fig. 14. (a) Elements in reconstructed microstructure, where the b and c boxes are areas which will be investigated in subfigures (b) and (c); (b) the delamination energy accumulation on the interface between Nafion and the C/Pt agglomerate at 60 s, where di represents the initiation position of the delamination; (c) the plastic Mises strain pattern at 1612 s, where ci represents the initiation position of crack in the Nafion.

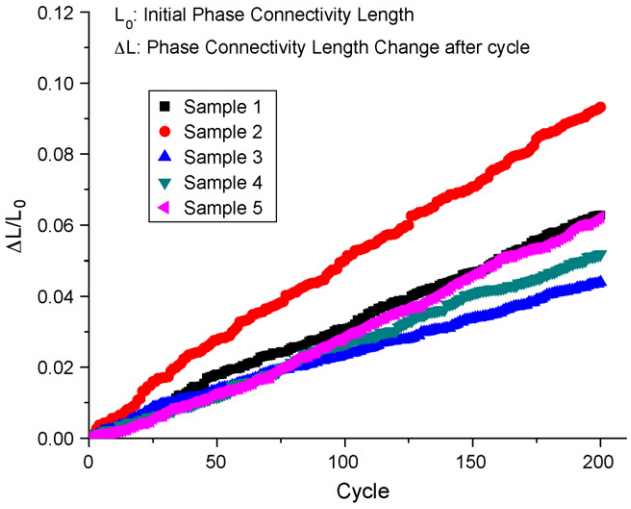


Fig. 15. The evolution of phase connection length between Nafion and the C/Pt agglomerate.

connectivity after 200 cycles for all five samples. Although there are various sample-specific microstructure changes in the five samples, the increase in connectivity change is a common feature and is a very important indication of the decay in performance.

These simulations clearly demonstrate that the mechanical mechanism underlying the microstructure changes for CLs is the competition between delamination energy accumulation on the interface between different solid phases and plasticity accumulation in the Nafion.

## 5. Conclusions

Based on experimental images of CLs, statistical features are extracted and are used to reconstruct the microstructure in CLs. The reconstruction process is accomplished in two steps. One is the filtering method, which changes the Gaussian distributed signals to three-phase microstructure reconstruction. The other is the stochastic optimization method, which refines the microstructure reconstruction to fit the statistical features of the experimental images.

To understand the underlying mechanical mechanism of microstructure changes, the reconstructed microstructure of CLs subjected to hydrothermal loading cycles is investigated. The mechanical analysis model developed in our companion paper [7] is extended to calculate the reconstructed microstructure changes. Numerical simulation shows that delamination and fracture phenomena do happen in the CLs after certain duty cycles of humidity and temperature, as the competition between the plasticity energy accumulation in the Nafion and the delamination energy accumulation on the interface between Nafion and the C/Pt agglomerate. Although different reconstructed microstructures show sample specific results, a common trend can be observed in the simulation results. That is, the cycled change of environment causes a decrease in connection between different solid phases, which may be an indication of performance degradation.

## Acknowledgments

The authors gratefully acknowledge the Nissan and NRC-IFCI collaboration program. Dr. Feng Rong appreciates the support of the Visiting Fellowships in Canadian Laboratories Program of the Natural Sciences and Engineering Research Council of Canada. All authors gratefully acknowledge the assistance of the referees who have provided so many valuable comments.

## References

[1] J. Xie, D.L. Wood, D.M. Wayne, T.A. Zawodzinski, P. Atanassov, R.L. Borupa, J. Electrochem. Soc. 152 (1) (2005) A104–A113.
[2] D.P. Wilkinson, J. St-Pierre, in: W. Vielstich, H.A. Gasteiger, A. Lamm (Eds.), Handbook of Fuel Cells: Fundamental, Technology and Applications, John Wiley & Sons, 2003.
[3] S.D. Knights, K.M. Colbow, J. St-Pierre, D.P. Wilkinson, J. Power Sources 127 (2004) 127–134.
[4] J. Xie, D.L. Wood, K.L. More, P. Atanassov, R.L. Borup, J. Electrochem. Soc. 152 (5) (2005) A1011–A1020.
[5] S. Kundu, M.W. Fowler, L.C. Simon, S. Grot, J Power Sources 157 (2) (2006) 650–656.
[6] A. Kusoglu, A.M. Karlsson, M.H. Santare, S. Cleghorn, W.B. Johnson, J. Power Sources (2006) 987–996.
[7] F. Rong, C. Huang, Z.S. Liu, D.T. Song, Q.P. Wang, J. Power Sources 175 (2008) 699–711.
[8] K.L. More, J. Bentley, K.S. Reeves, http://www.hydrogen.energy.gov/pdfs/progress06/v_g_3_more.pdf, 2006.
[9] J.R. Wilson, W. Kobsiriphat, R. Mendoza, H.-Y. Chen, J.M. Hiller, D.J. Miller, K. Thornton, P.W. Voorhees, S.B. Adler, S.A. Barnett, Nat. Mater. 5 (2006) 541–544.
[10] P.M. Partha, W. Chao-Yang, J. Electrochem. Soc. 153 (2006) pA840.
[11] P.M. Adler, J.-F. Thovert, S. Bekri, F. Yousefian, J. Eng. Mech. 128 (8) (2002) 829–839.
[12] S. Torquato, Ann. Rev. Mater. Res. 32 (2002) 77–111.
[13] P.M. Adler, C.G. Jacquin, J.A. Quiblier, Int. J. Multiphase Flow 16 (4) (1990) 691–712.
[14] D. Cule, S. Torquato, J. Appl. Phys. 86 (6) (1999) 3428–3437.
[15] Z. Xie, T. Navessin, K. Shi, R. Chow, Q. Wang, D. Song, B. Andreaus, M. Eikerling, Z. Liu, S. Holdcroft, J. Electrochem. Soc. 152 (6) (2005) A1171–A1179.
[16] G. Marsaglia, A. Zaman, Ann. Appl. Probab. 3 (1991) 462–480.
[17] N. Losic, J.-F. Thovert, P.M. Adler, J. Colloid Interface Sci. 186 (2) (1997) 420–433.
[18] M.Y. Joshi, University of Kansas, 1974.
[19] R. Brent, Algorithms for Minimization Without Derivatives, Prentice-Hall, 1973.
[20] C.L.Y. Yeong, S. Torquato, Phys. Rev. E 57 (1998) 495–506.
[21] C.L.Y. Yeong, S. Torquato, Phys. Rev. E 58 (1998) 224–233.
[22] M.D. Rintoul, S. Torquato, J. Colloid Interface Sci. 186 (1997) 467–476.
[23] S. Mazur, G.W. Foggin, C.E. Jackson, ECS National Meeting, 2006.
[24] Y. Tang, A.M. Karlsson, M.H. Santare, M. Gilbert, S. Cleghorn, W.B. Johnson, Mater. Sci. Eng. A 425 (2006) 297–304.